Supplementary Information for

Migration-assisted, Moisture Gradient Process for Ultrafast, Continuous CO_2 Capture from Dilute Sources at Ambient Conditions

Aditya Prajapati[1], Rohan Sartape[1], Tomás Rojas[2], Naveen K. Dandu[2], Pratik Dhakal[3], Amey S. Thorat[3] ,Jiahan Xie[4], Ivan Bessa[5], Miguel T. Galante[5], Marcio H. S. Andrade[5], Robert T. Somich[4], Marcio V. Reboucas[5], Gus T. Hutras[4], Nathalia Diniz[5], Anh T. Ngo[1, 2], Jindal Shah[3], Meenesh R. Singh[1*]

[1] Department of Chemical Engineering, University of Illinois at Chicago, 929 W. Taylor St., Chicago, Illinois, USA 60607
[2] Material Sciences Division, Argonne National Laboratory, 9700 S Class Ave, Lemont, Illinois, USA 60439
[3] Department of Chemical Engineering, Oklahoma State University, 420 Engineering North, Stillwater, Oklahoma, USA 74078
[4]Braskem America Inc., 550 Technology Drive, Pittsburgh, PA, 15219
[5]Braskem S.A, Rua Eteno S/N, Camaçari, Bahia, Brazil

Table of Contents

S1. Experimental methods

This section describes the details for calibration of the concentration of $HCO_3^-$and CO_3^{2-}using Fourier transform Infrared spectroscopy (FTIR), determining H_2O concentration using Karl Fisher (KF) titrations, dynamics of CO_2 capture experiments on the organic side, and the migration-assisted moisture-gradient (MAMG) experiments for CO_2 capture.

S1.1 Fourier Transform Infrared (FTIR) Spectroscopy

FTIR spectroscopy was performed to estimate the HCO_3^- - CO_3^{2-}equilibrium in water-deprived conditions. All the experiments were performed on a Bruker Invenio S bench using a Pike VeeMax II variable angle accessory and a 60° Ge face-angled crystal for the attenuated total reflectance (ATR) measurements with a Jackfish ATR spectroelectrochemical cell mounted on top of the accessory to contain the organic solution. A mid-band liquid N_2- cooled mercury cadmium telluride (MCT) detector was used for higher sensitivity in analyzing liquid samples. The spectra acquired were averaged over 1500 scans at a resolution of 4 cm^{-1}. The organic phase used for these experiments was CH_3OH. The reason for choosing CH_3OH over ethylene glycol (EG) was strictly for the purpose of acquiring cleaner spectra as vibrations of the moieties in EG interfered with the detection of HCO_3^- and CO_3^{2-}. The intensity of the HCO_3^- band at 1633 cm^{-1} and the CO_3^{2-} band at 1450 cm^{-1} were individually calibrated at different concentrations of HCO_3^- and CO_3^{2-} in CH_3OH. The experimental setup can be seen in Figure S. 1.

Figure S. 1 Experimental setup for FTIR measurements using a PikeVeeMax II ATR accessory and a 60o face-angled Ge crystal. The known amounts of $NaHCO_3$or Na_2CO_3 are added to CH_3OH contained in the Jackfish cell.

Initially, background spectra were acquired using only CH_3OH in the cell to minimize the influence of CH_3OH peaks during the actual HCO_3^- - CO_3^{2-}equilibrium studies.A known amount of $NaHCO_3$ was added to the cell with pure CH_3OH and was allowed to dissolve. Once the clear solution was obtained, the spectra of this solution were acquired, and the intensity was at 1633 cm^-

[1]. This process was repeated for increasing amounts of $NaHCO_3$ in CH_3OH. The increase in $NaHCO_3$also increased the intensity of the 1633 cm^{-1}peak, and thus, HCO_3^- concentration was calibrated using this intensity.

Similarly, in a separate set of experiments, a known amount of Na_2CO_3 was added to pure CH_3OH to establish a calibration curve for $CO_3^{2-}$with the intensity at 1450 cm^{-1}. The calibration curves for both $NaHCO_3$and $Na_2CO_3$are shown in Figure S. 2. Once the calibrations were complete, a known amount of NaOH was added to pure CH_3OH, and CO_2 was sparged into the Jackfish cell to convert the OH^- into HCO_3^-. Since Na^+ is just a spectator ion, it doesn't participate in the reaction and the intensities obtained from the calibrations of $NaHCO_3$and Na_2CO_3can be directly used to find the concentrations of $HCO_3^-$and CO_3^{2-}. At this point, HCO_3^-peaks can be observedin the spectra, and only when a known amount of water to the cell, CO_3^{2-} peaks are observed, as seen in Figure 2A of the manuscript.

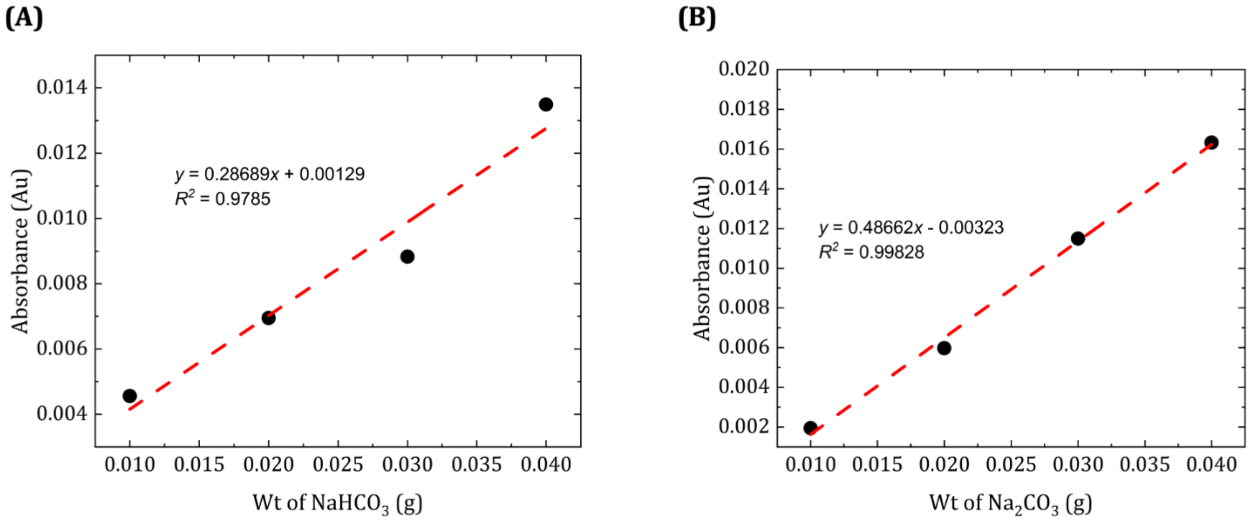

Figure S. 2: FTIR calibration of intensity vs. the known amounts of (A) $NaHCO_3$and (B) Na_2CO_3.

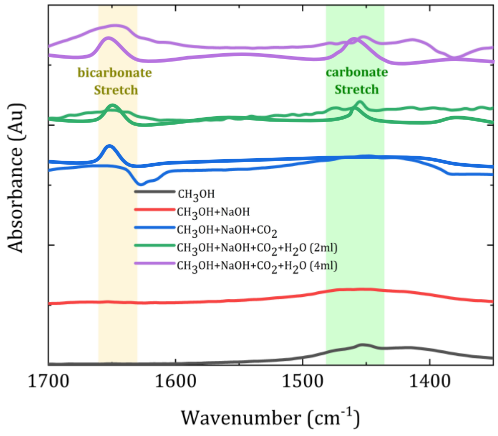

Figure S. 3: FTIR inset of the bicarbonate and carbonate stretching.

Figure S. 3 shows the inset between 1300-1700 cm^{-1}. When the CO_2 sparging starts, HCO_3^- stretches start appearing at 1633 cm^{-1} indicating the formation of HCO_3^-. As the water is added to the system, the CO_3^{2-} stretches at 1450 cm^{-1} become more intense confirming the influence of water in this equilibrium.

S1.2 Karl Fisher (KF) Titrations

KF titrations were performed to find the total water content while studying the HCO_3^--CO_3^{2-} equilibrium in water-deprived conditions. FTIR spectroscopy helps in determining the concentration of $HCO_3^-$and CO_3^{2-} species but since the vibrational peaks of the added water are too intense to distinguish from the water produced due to the shift in the equilibrium from HCO_3^- to CO_3^{2-}, KF titrations were necessary to estimate the water content to precisely determine the dependence of the HCO_3^--CO_3^{2-}equilibrium on the concentration of water. A custom-made 3D-printed cell of the same capacity as the Jackfish cell used in the FTIR was used for this study. A solution of CH_3OH, $NaHCO_3$, and a known amount of H_2O in the cell was well mixed using a magnetic stirrer. Two Cu electrodes were placed on the opposite ends of the cell, and the cell's open circuit potential (OCP) was constantly monitored. 20 µl of KF titrant was added to the cell periodically, and the endpoint was detected by a sharp increase in the OCP of the cell. This potentiometric endpoint is an indicator of the total H_2O in the solution.Figure S. 4 shows the endpoint detection using the OCP measurement technique.

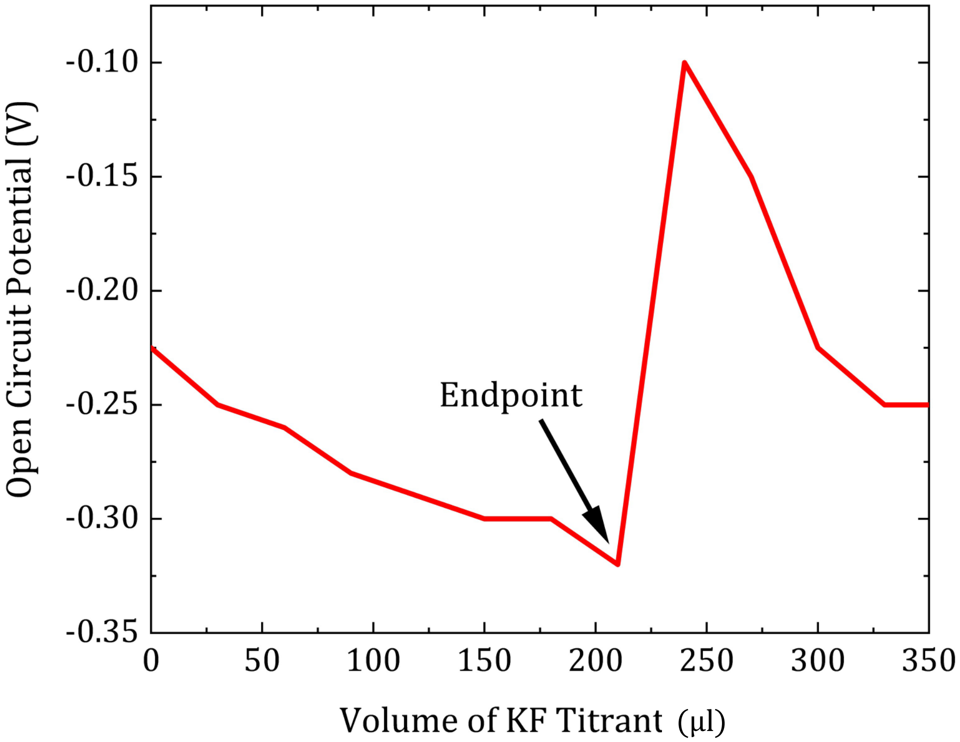

Figure S. 4: Potentiometric endpoint detection of KF titration from the sharp change in OCP.

The water evolved due to the equilibrium shift can be measured as:

$$V_{eq} = V_{KF} - V_{added} \tag{1}$$

where V_{eq} is the volume of water produced due to the equilibrium shift, V_{KF} is the volume of water detected by KF titration and V_{added} is the known volume of water added to drive the shift in the equilibrium.V_{KF} is determined by the stoichiometry of the KF reaction:

$$I_2 + SO_2 + H_2O \rightarrow SO_3 + 2HI \tag{2}$$

where $I_2 + SO_2$ are the main ingredients of KF titrant that reacts with H_2O. Once the entire H_2O is consumed, the sharp increase in the OCP is observed, and the endpoint is determined from the stoichiometry as 1 mol of I_2 reacting with 1 mol of H_2O. Subsequently, the equilibrium constant is determined by:

$$K = \frac{[CO_2][CO_3^{2-}][H_2O]}{[HCO_3^-]^2} \approx \frac{[CO_3^{2-}]^2[H_2O]}{[HCO_3^-]^2} \tag{3}$$

S1.3 CO_2 capture on the organic side

On the organic side of the MAMG setup, CO_2 is continuously sparged into the organic side containing 1.2M KOH dissolved in ethylene glycol (EG), which is a CO_2 binding organic liquid (CO2BOL). The sparged CO_2 is converted into HCO_3^- by:

$$CO_2 + OH^- \leftrightharpoons HCO_3^- \tag{4}$$

This rate of this CO_2 capture reaction and, consequently, the concentration of HCO_3^- was monitored by observing the change in the solution resistance of the CO2BOL using electrochemical impedance spectroscopy (EIS).The calibration curveseen in Figure 3A of the manuscript was createdwith varying concentration mixtures of KOH and $KHCO_3$ in CO2BOL, keeping the concentration of K^+ constant. EIS was performed on each of these solutions with a 20mV sinusoidal pulse in the frequency range of 100 kHz to 30 Hz. Figure S. 5 shows Randles circuit Nyquist plot as a consequence of EIS at different concentration ratios ofKOH and $KHCO_3$in CO2BOL.

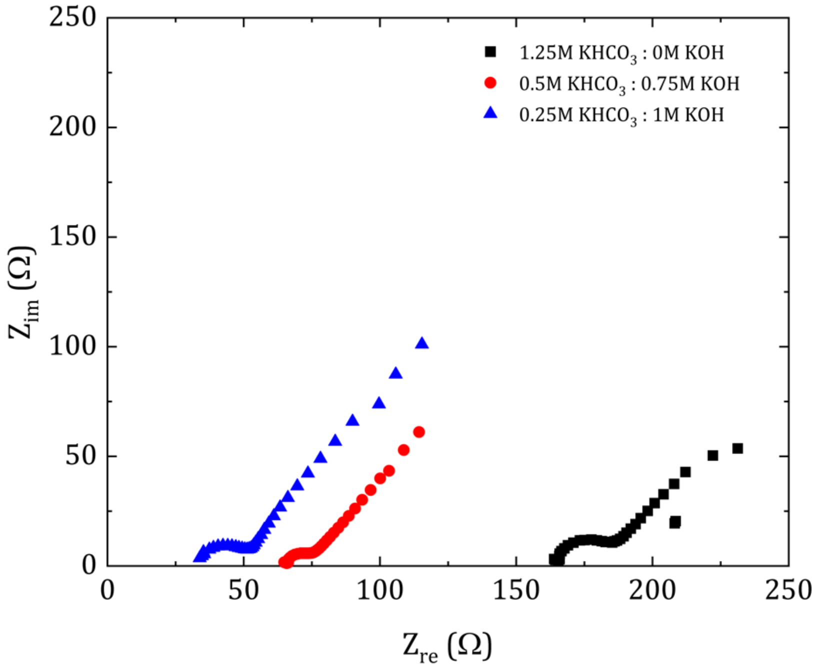

Figure S. 5: Nyquist plot from EIS for different concentration ratios of KOH and $KHCO_3$.

S1.4 MAMG experiments

MAMG experiments were performed to capture CO_2 at a record high flux. Figure S. 6shows a detailed schematic of the entire process. CO_2 is sparged into the organic side where it is chemisorbed by the1.2M KOH solution in CO2BOL to form HCO_3^-. An anion exchange membrane (AEM) separates the organic side from the aqueous, initially comprising 0.1M KOH. The separation of the organic and aqueous sides creates a moisture gradient across the AEM, which initially drives the HCO_3^-diffusionacross the AEM.

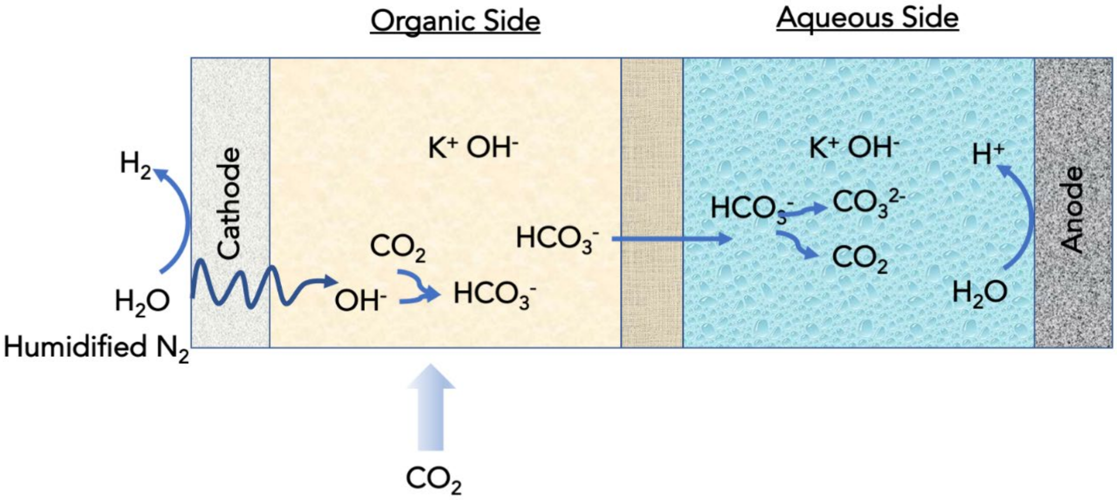

Figure S. 6: A detailed schematic of MAMG

On the aqueous side, the diffused HCO_3^- converts back to CO_2 and CO_3^{2-} thereby reducing the pH of the alkaline aqueous medium. This moisture-gradient facilitated transfer of HCO_3^- is accelerated by establishing an electric field across the device. The cathode on the organic side is supplied with humidified N_2 and acts as a gas diffusion electrode to reduce water to H_2 and serves as a constant source to generate OH^- thereby increasing the CO_2 uptake. The aqueous side is anodic and attracts the HCO_3^- ions, further enhancing the rate of transfer of HCO_3^- and CO_2 release on the aqueous side.

S2. Computational methods

S2.1 Density Function Theory (DFT) methods

To determine the ΔG of HCO_3^- going to CO_3^{2-}, CO_2, and H_2O in the solvent, DFT calculations were performed using B3LYP(1-3) functional with 6-31+G(2df,p) basis set utilizing Gaussian09 software code.(4) For performing calculations in the presence of a solvent, we used the Polarizable Continuum Model (PCM)(5) by specifying the static (or zero-frequency) dielectric constant (ϵ) of the solvent mixture (water +EG) at different concentrations. At each volume of water added, we obtained a different value of ϵ using the formulation developed by Jouyban and Soltanpour (6). In this methodology, the ϵ of a solution is calculated based on the individual ϵ of the solvents as well as their Abraham solvation parameters. At each of the ϵ values, DFT optimization and solvent calculation of the reactants and products were performed and Gibbs free energies of each of the species were used to calculate ΔG of the reaction. We estimate the $\epsilon$for a solution of ethylene glycol with different volumes of added water as shown in Table S.1.

Table S. 1ϵvalues for the water/ethylene glycol solution for different volumes of added water.

Volume of water added (ml)	Mole fraction of water (x_W)	Mole fraction of ethylene glycol (x_{EG})	ϵ
0	0	1	37
0.1	0.072	0.928	39.834
0.2	0.135	0.865	40.968
0.3	0.189	0.811	42.077
0.4	0.237	0.763	43.197

At each of these ϵvalues, we performed DFT optimization and solvent calculations of each of the reactants and products. We then used following formula to determine ΔG of the reaction:

$$\Delta G = \Sigma G_{products} - \Sigma G_{reactants}; G = Gibbs\ free\ energy\ in\ solution \qquad (5)$$

S2.2 Multiphysics modeling using COMSOL

A one-dimensional model for the $MAMGCO_2$ capture system was developed using COMSOL Multiphysics to solve the Nernst-Planck equation for the transport of different ionic species to evaluate the performance of such a system by varying operating parameters such as migration current, membrane thickness, and relative humidity of the CO_2 feed. The experimentally obtained equilibrium constant under water-deprived conditions and the dynamics of CO_2 capture with the rate of HCO_3^- formation in the organic side were used to emulate realistic conditions in the model.

Transport of species: Only diffusion and ionic mobility due to the applied electric field were assumed to drive the species' transport in the absence of convection. The diffusion of the ions (H^+, K^+, OH^-, HCO_3^-, CO_3^{2-}) and CO_2 in the aqueous side are shown inTable S. 2. We neglect the variation of diffusion coefficients with the electrolyte concentration, as the variation is marginal for dilute electrolytes (<< 10 mol%).

Table S. 2: Diffusion coefficients of species in water at infinite dilution at 25 °C(7)

Species	**Diffusion Coefficient (10^{-9} m^2 s^{-1})**	**Mobility (10^{-7} m^2 V^{-1} s^{-1})**
CO_2	1.91	-
HCO_3^-	1.185	0.462
CO_3^{2-}	0.923	0.359
H^+	9.311	3.626
OH^-	5.273	2.054
K^+	1.957	0.762

Since the concentration of water in the water-deprived environment facilitates the transport mechanism in the organic side and across the membrane, the diffusion was also dependent on the water uptake λ of the membrane(8, 9).The diffusion coefficient of water and CO_2 in the organic side are given in

Table S. 3: Diffusion coefficients in EG(10, 11)

Species	**Diffusion Coefficient (10^{-9} m^2 s^{-1})**
CO_2	0.300
H_2O	0.375

The governing equation used in the model was:

$$\frac{\partial C_j}{\partial t} + \nabla \cdot \mathbf{J_j} = R_j \tag{6}$$

where C_j is the concentration, $\boldsymbol{J_j}$is the flux, and R_j is the reaction rate of the of the jthspecies. The total diffusive and ionic mobility flux is given by:

$$J_j = -D_j \nabla C_j - z_j u_{m,j} F C_j \nabla V \tag{7}$$

where D_j is the λ dependent diffusion coefficient $D_j(\lambda)$, (8, 9, 12-14)z_j is the charge number, $u_{m,j}$ is the ionic mobility of the jth species. F is the Faraday's constant and V is the potential.

Reactions on the organic side: The moisture-gradient CO_2 capture is implemented using water-dependent CO_3^{2-} - HCO_3^- equilibrium reactions. The H_2O dissociation reaction considered in the model is:

$$H_2O \overset{k_w}{\Leftrightarrow} H^+ + OH^- \tag{8}$$

The CO_3^{2-}-HCO_3^- equilibrium reactions are given by:

$$CO_2 + OH^- \overset{k_1}{\Leftrightarrow} HCO_3^-$$
$$CO_2 + H_2O + CO_3^{2-} \overset{k_2}{\Leftrightarrow} 2HCO_3^- \qquad (9)$$

The same reactions are also considered on the aqueous side but the activity of water is taken as unity, and the reactions are treated simply as aqueous CO_3^{2-}-HCO_3^- equilibrium reactions with well-defined forward and backward rate constants. (15)

Membrane: The anion exchange membrane (AEM) such as Snowpure Excellion was modeled as a solid electrolyte of thickness between 50-150 μm thickness with a fixed concentration of background positive charge of 1 M. Since there is a gradient of moisture across the membrane the diffusion coefficients of anions and cations used are dependent on the concentration of water and change as a function of membrane's water uptake λ(8, 9, 12-14).

Charge transfer reactions at Anode and Cathode: The charge-transfer kinetics at the anode and cathode were modeled using the expression for Tafel kinetics, such as

$$i_s = i_l = i_R = i_0 \exp\left(\frac{\alpha F \eta}{RT}\right) \qquad (10)$$

where i_s is the electrode current density, i_R is the reaction current density, i_0 is the exchange-current density, and α is the transfer coefficient. The kinetic overpotential of a catalyst is given by $\eta = \phi_s - \phi_l - E^0 + \Delta\phi_{\text{Nernstian}}$, where E^0 is the equilibrium potential of the half-reaction at standard condition and, ϕ_s is the electrode potential.

The half-cell reaction at the anode on the aqueous side is the oxidation of water, which creates acidic conditions near the electrode.

$$\mathrm{H_2O} \rightarrow \frac{1}{2}\mathrm{O_2} + 2\mathrm{H^+} + 2\mathrm{e^-}, \quad E^0 = 1.229\,\mathrm{V} \qquad (11)$$

The other half-cell reactions atthe cathode on the organic side involve the reduction water coming from the humidified N_2 on the carbon electrode that acts as a gas diffusion electrode. It not only reduces water to H_2 but also produces OH^- thereby constantly providing a source for CO_2 capture in CO2BOL at the organic side. As shown below, the reduction of water can be written as:

$$2\mathrm{H_2O} + 2\mathrm{e^-} \rightarrow \mathrm{H_2} + 2\mathrm{OH^-} \qquad E^0 = 0\,\mathrm{V} \qquad (12)$$

Migration Current*:* The current density at the electrodes is given by Ohm's law:

$$i_s = -\kappa_s \frac{\partial \phi_s}{\partial x} \qquad (13)$$

where κ_s is the conductivity of the electrode.

To maintain electroneutrality, the divergence of current density in the solid and the liquid must be zero:

$$\frac{\partial i_l}{\partial x} = 0, \quad \frac{\partial i_s}{\partial x} = 0 \tag{14}$$

The potential in the electrochemical cell was calculated relative to the zero potential of electrolyte at cathode-electrolyte interface and the migration current is a parameter chosen from the experiments and is implemented on the anodic side in the model as:

$$-\boldsymbol{n} \cdot \boldsymbol{i} = i_0 \tag{15}$$

where $\boldsymbol{i}$ is the current density vector and $\boldsymbol{i}$ of CO_2 utilization, $-\boldsymbol{n}$ is the normal vector pointing inward, and i_0 is the migration current value from the experiments. Equations (6)-(15) were solved using COMSOL Multiphysics 5.2a to study the time-dependent evolution of the concentration of the ionic species and CO_2 with varying process parameters such as migration current, membrane width, and CO_2 feed relative humidity.

S3. Calculating CO$_2$ concentration from pH

MAMG CO$_2$ capture performance was measured by observing the drop in the pH of 0.1M KOH on the aqueous side due to the migration of HCO$_3^-$ and its conversion to CO$_2$ and CO$_3^{2-}$. Using the well-established aqueous equilibrium relationship of these species, the CO$_2$ concentration was calculated using pH as follows:

The equilibrium constants are obtained from these aqueous reactions:

$$\begin{gathered} CO_2 + OH^- \leftrightharpoons HCO_3^- \quad (K_{1,aq} = 10^{7.63}\ l/mol) \\ CO_2 + H_2O + CO_3^{2-} \leftrightharpoons 2HCO_3^- \quad (K_{2,aq} = 10^{3.88}) \end{gathered} \tag{16}$$

Using the above relationship, the HCO_3^- and CO_3^{2-} concentrations can be expressed in terms of CO$_2$ as:

$$[HCO_3^-] = K_{1,aq} \times [CO_2][OH^-]$$

$$\begin{aligned} [CO_3^2 -] &= \frac{[HCO_3^-]^2}{K_{2,aq} \times [CO_2]} = \frac{\left(K_{1,aq} \times [CO_2][OH^-]\right)^2}{K_{2,aq} \times [CO_2]} \\ &= K_{1,aq}^2 \times \frac{[CO_2][OH^-]^2}{K_{2,aq}} \end{aligned} \tag{17}$$

Imposing electroneutrality on the aqueous side, the total ionic balance can be written as:

$$\Sigma_i z_i C_i = 0 \tag{18}$$

where z_i is the charge of the ionic species and C_i is the concentration of the species. The electroneutrality equation can be expressed in terms of the ionic species on the aqueous side as:

$$[K^+] + [H^+] - [OH^-] - [HCO_3^-] - 2[CO_3^{2-}] = 0$$

$$\begin{aligned} &[K^+] + [H^+] - [OH^-] - K_{1,aq} \times [CO_2][OH^-] - 2K_{1,aq}^2 \times \frac{[CO_2][OH^-]^2}{K_{2,aq}} \\ &= 0 \end{aligned} \tag{19}$$

The only unknown in eq. (19) is $[CO_2]$ as $[K^+] = 0.1M$ being the spectator ion that doesn't participate in the equilibrium reactions, $[H^+] = 10^{-pH}M$, and $[OH^-] = 10^{pH-14}M$.

S4. Techno-economic analysis

To realize the feasibility of a MAMG CO_2 capture process, a detailed assessment of the capital and operating costs was performed. This analysis was performed for the basis of capturing CO_2 at the rate of 1000 ton/hr. The MAMG CO_2 capture has a maximum flux of capturing 2.3 mmol/m^2/s of CO_2 in a lab-scale setup. This flux can be maintained on a larger scale if the area required is scaled up to match the CO_2 capture capacity of the lab-scale MAMG CO_2 capture. This can be calculated by:

$$A_{reqd} = \frac{Capacity}{flux_{MAMG}} \qquad (20)$$

where $\mathrm{A_{reqd}}$ is the area required for the larger setup, $\mathrm{Capacity} = 1000\ \mathrm{ton/hr}$ is the CO_2 capture capacity taken as the basis for the techno-economic analysis and $\mathrm{flux_{MAMG}} = 2.3\ \mathrm{mmol/m^2s}$ is the maximum CO_2 capture flux obtained in our MAMG CO_2 capture process. Using these values, the total area required is calculated to be ~2744840 m^2.

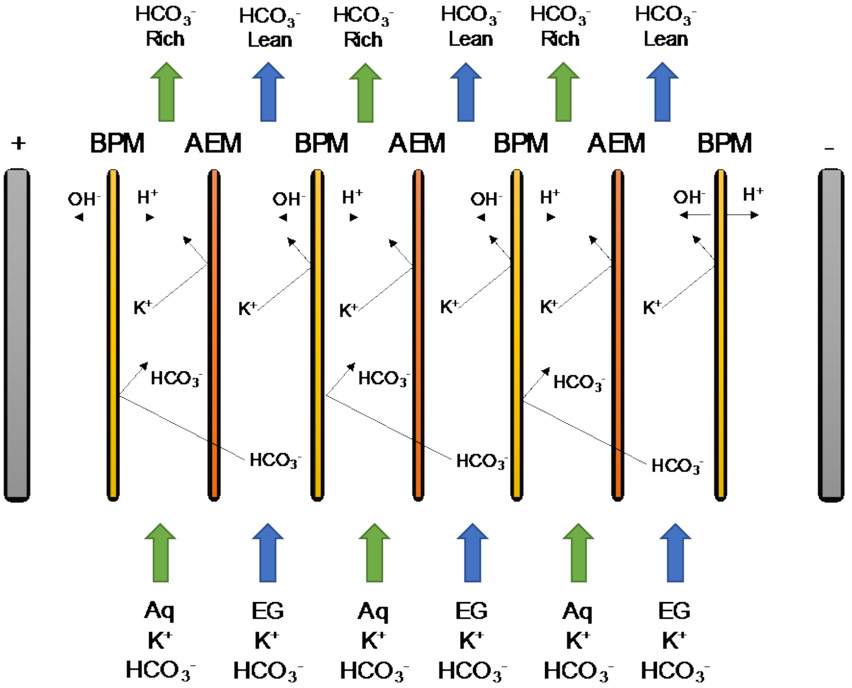

Figure S. 7: Schematic representation of an ED stack for scaling up of a MAMG CO_2 capture process

The electrodialysis (ED)-type systems are scaled up using stacks of multiple single-unit ED systems which are similar to the one shown in Figure S6. A typical commercially available ED stack system is represented in Figure S. 7. One such ED stack comprises many parallel cells that can be simultaneously used for the MAMG CO_2 capture. The HCO_3^- ions migrate to the aqueous side from the organic side comprising of ethylene glycol (EG) that acts as the CO_2 binding organic liquid. Further migration of HCO_3^- ions is inhibited by using a bipolar membrane (BPM) such that HCO_3^- ions concentrate only in the aqueous parts of the stack. This stack-type arrangement allows using 2 electrodes for all the cell-pairs in between the electrodes. Specifications of a typical ED stack system provided by Lenntech Water Treatment Solutions are given in Table S. 4.

Table S. 4: Specification of a commercial ED stack system

Parameter	**Value**
Membrane Area	0.2 m^2
ED cell pairs/stack	512 units
Rated operating current density	250 A/m^2
Rated operating voltage	300 V

With each cell in the ED stack having the membrane area of 0.2 m^2, the total membrane area per stack can be calculated as:

$$\begin{aligned} \mathrm{A_{mem,stack}} &= \mathrm{A_{cell}} \times \mathrm{n_{cell}} = 0.2 \times 512 \\ &= 102.4\ \mathrm{m^2} \end{aligned} \tag{21}$$

where $\mathrm{A_{mem,stack}}$ is the area of membrane for the whole stack, $\mathrm{A_{cell}} = 0.2\ \mathrm{m^2}$ is the area of membrane for each cell, and $\mathrm{n_{cell}} = 512$ is the number of cells in a whole stack of ED system. Since the total area determined from eqn (20) is 2744840$m^{2,}$ and the area of membranes in one whole stack is determined from eqn (21) as 102.4 m^2, the number of full ED stacks required can be obtained by:

$$\mathrm{n_{stacks}} = \frac{\mathrm{A_{reqd}}}{\mathrm{A_{mem,stack}}} \approx 26805 \tag{22}$$

Hence, 26805 full ED stacks of the given specifications will meet the area requirements to capture 1000 ton/hr of CO_2. Since each stack can be operated at a maximum rated current density of 250 A/m^2, it is imperative to determine if the ED stack can sustain the capture flux of 2.3 $mmol/m^2/s$ with this limit. The current density required to maintain this flux can be calculated as:

$$I_{reqd} = flux_{MAMG} \times F \times 1000 = 221.92\ A/m^2 \tag{23}$$

where $\mathrm{I_{reqd}}$ is the current density required to maintain the MAMG CO_2 capture flux, F is the Faraday's constant, for the final quantity in A/m^2. The total $\mathrm{I_{reqd}} = 221.92\ \mathrm{A/m^2}$. This value is within the maximum rated operating current density of the ED stack, and hence, the stack can maintain the MAMG capture flux and is a suitable candidate for scaling up the MAMG process.

The total cost of this large-scale MAMG stack can be divided into two parts- 1) Captial expense: Primarily include the cost of the stack and the cost of the membrane. 2) Operating expense: Primarily includes the cost of electricity. Table S. 5 shows the major costs incurred as capital expenses

Table S. 5: Major capital expenses for scaling up MAMG CO_2 capture technique

Component	**Cost**	**Lifetime**	**Source**
ED Stack	\$500,000/stack	25 years	LennTech
AEM	\$ 20/m^2	3-8 years	Sabatino et al.(16)
BPM	\$100/m^2	3-8 years	Sabatino et al.(16)

Since the CO_2 capture basis is taken as the mass of CO_2 captured per hour, it is fitting to express the costs per hour as well. Hence, with a conservative estimate of the ED stack with membranes operating at 50% efficiency, the total capital expense rate of the ED stack can be calculated as:

$$C_{stack} = n_{stacks} \times \frac{C_{ED}}{LT_{ED} \times 8760 \times \eta} \approx \$122{,}400\ /hr \tag{24}$$

where C_{stack} is the capital expense rate of ED stacks, $C_{ED} = \$500{,}000$ is the cost of one whole ED stack system, $LT_{ED} = 25\ years$ is the lifetime of the ED stack, factor to represent the final quantity in \$/hr and $\eta = 50\%$ is the efficiency of operation. The total capital expense rate of the ED stacks is \$122,400/hr. Two membranes (AEM and BPM) are used on either side of the organic phase for one cell in the ED system. Hence, the capital expense rate of membranes is calculated as:

$$C_{mem} = \frac{(C_{AEM} + C_{BPM}) \times A_{reqd}}{LT_{mem} \times 8760 \times \eta} \approx \$15040/hr \tag{25}$$

where C_{mem} is the capital expense rate of membranes, $C_{AEM} = \$20\ /m^2$ is the unit price of AEM, $C_{BPM} = \$100\ /m^2$ is the unit price of BPM, assuming an average lifetime of membranes $LT_{mem} = 5\ years$, $\eta = 0.5$ is the operation efficiency, and 8760 is the unit conversion factor to represent the final quantity in \$/hr. The total capital expense rate is then obtained as:

$$C_{capex} = C_{stack} + C_{mem} = \$137440\ /hr \tag{26}$$

where C_{capex} is the capital expense rate of the scaled-up MAMG CO_2 capture process.

The operating cost of this process primarily arises from electricity consumption. This energy consumption can be calculated by:

$$E_{MAMG} = I_{reqd} \times A_{electrode} \times V_{rated} \times n_{stacks} \times 1hr = 357\ MWh \tag{27}$$

where $A_{\text{electrode}} = 0.2\ \text{m}^2$ is the area of the electrodes, $V_{\text{rated}} = 300\ \text{V}$ is the rated operating voltage of the ED stack, as seen from Table S. 4. With a standard cost of electricity \$20/MWh, the rate of operating expense can be calculated by:

$$C_{opex} = E_{MAMG} \times C_{elec} \approx \$\ 7140\ /hr \tag{28}$$

where C_{opex} is the operating expense rate and $C_{\text{elec}} = \$20/\text{MWh}$ is the cost of electricity. The total cost of establishing and operating the scaled-up MAMG CO_2 capture plant is the sum of the C_{capex} and C_{opex} from eqns. (26) and (28). The total cost is:

$$\text{C}_{\text{total}} = \text{C}_{\text{capex}} + \text{C}_{\text{opex}} \approx \$144{,}575/\text{hr} \tag{29}$$

For a capacity of capturing 1000 ton CO_2/hr, the cost of CO_2 capture is:

$$\text{C}_{\text{CO}_2} = \frac{\text{C}_{\text{total}}}{\text{Capacity}} = \$144.5/\text{ton CO}_2 \tag{30}$$

S5. Effect of Impurities and long-term stability of MAMG CO_2 capture

The study of the effect of impurities and the long-term stability of the reported method are crucial in understanding the versatility and feasibility of scalingup this process. To test the effect of impurities, a flue gas feed consisting of 71% N_2, 19% O_2, >9% of CO_2, and <1% of SO_X was sparged into the MAMG CO_2 capture cell. Figure S. 8 shows the influence of these additional impurities. It can be seen from the figure that the performance of the MAMG CO_2 capture technique is similar to the performance in the absence of impurities. This indicates that the system retains its performance in the presence of the impurities most commonly seen in flue gas at the exhaust of a coal-fired boiler or a power plant.

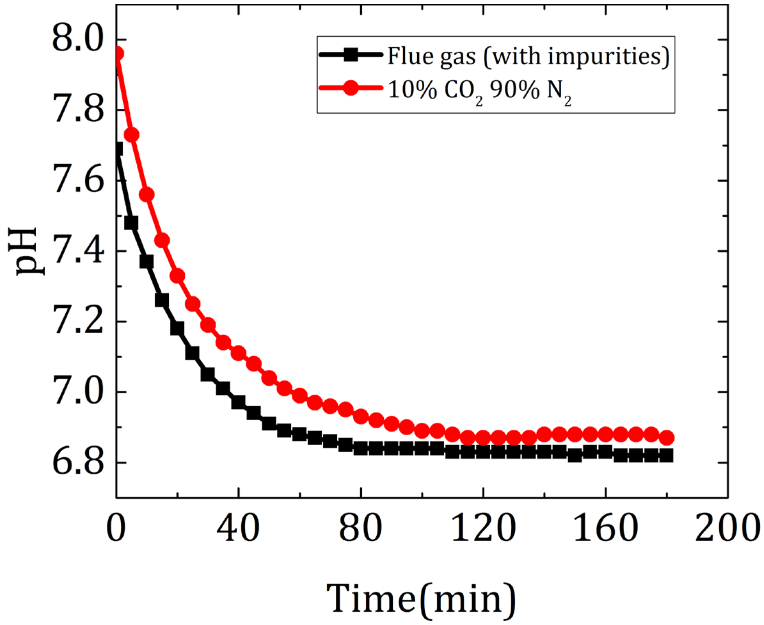

Figure S. 8: MAMG CO_2 capture performance under the influence of impurities.

A long-term MAMG CO_2 capture experiment was performed for a duration of 16 hours, as seen in Figure S. 9. The aqueous solution is replenished during this long-term experiment. As can be seen from this figure, thecapture process remains stable. Therefore, the MAMG CO_2 capture shows a reliable performance in the presence of impurities and can withstand long-term operation.

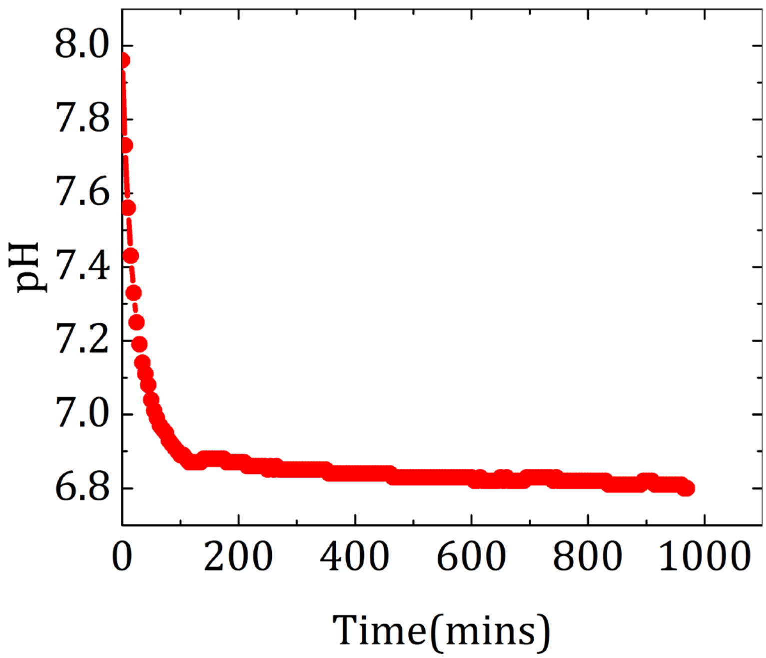

Figure S. 9: Long-term stability of the MAMG CO_2 capture process

S6. Machine learning-driven prediction of the performance of MAMG CO_2 capture

Data collection and processing:
COMSOL Multiphysics was used to obtain CO_2 capture efficiency and CO_2 saturation values under 176 operating conditions, with different CO_2 utilization current, migration current density, membrane thickness, and relative humidity values. The data was then carefully examined for any outliers and inconsistencies. We limited the data to operating conditions with predicted CO_2 capture efficiency and CO_2 saturation below 100%. The resulting dataset containing 126 data points was used to develop the machine learning models.

Feature selection and correlation:
In the next step, we examined the feature space for multicollinearity. Every feature was tested against every other feature, and none yielded correlation coefficients greater than 0.2. This confirmed that the feature space was free from multicollinearity. All four features were included in model development.

Data scaling and normalization:
Individual features often possess values that are orders of magnitude different from those of other features. For example, in this study, membrane thickness varied between 50 to 140 μm, while relative humidity between 0.2 to 0.8, thereby creating a difference of over three orders of magnitude between the smallest and largest feature values. Data scaling becomes essential to mitigate any biases that may arise due to such variation in feature values and improve the model performance. To achieve this, we used MinMaxScaler, implemented in sci-kit learn, to normalize the input features and outputs. MinMaxScaler transforms the values between 0 and 1, where 0 is the minimum value and 1 is the maximum value of the feature.

Multiple linear regression (MLR):
We implemented the MLR algorithm because of its simplicity and direct physical relevance. Linear models as shown in eqn. (31) and (32) were developed using MLR.

$$y1 = a1 * x1 + a2 * x2 + a3 * x3 + a4 * x4 \tag{31}$$

$$y2 = b1 * x1 + b2 * x2 + b3 * x3 + b4 * x4 \tag{32}$$

where y1 and y2 represented CO_2 capture efficiency and CO_2 saturation, respectively. The features were denoted using x1 through x4, such that CO_2 utilization is x1, CO_2 migration current density as x2, membrane thickness as x3, and relative humidity as x4. The linear model coefficients were represented using a1 through a4 and b1 through b4 as denoted in the equations.

Neural Network (NN):
NN method is a very powerful and complex machine learning algorithm inspired by the working mechanism of the neurons in our brain. The model consists of the input layer that takes in input information, passes on to the second layer known as the hidden layer that consists of several neurons that process the information, and passes it to the final layer known as the output layer that outputs the final prediction.

Hyperparameter Tuning:
Hyperparameters for the NN were found using the Randomized cross-validation method over a large parameter space evaluated using 5-fold cross-validation to reduce overfitting. The hyperparameter was found to be as follows: Layers: 2, Neurons: 18, Learn Rate: 0.009, Activation Function: Relu.

ML Results:
The distribution of model coefficients and R^2 values obtained from 20 random trials is given in Table S. 6.

Table S. 6: Summary of the model coefficients and mean R^2 values of MLR model over all the train/test iteration.

Coefficients and mean R^2 values for CO_2 capture efficiency

	a1	a2	a3	a4
Min	0.9472	-0.3500	-0.0786	0.0130
Max	1.1373	-0.1936	0.0356	0.3581
Mean	1.0570	-0.2775	-0.0197	0.1939
Std. Dev	0.0531	0.0393	0.0306	0.0959

	R^2
Test Data	0.7755
Train Data	0.8318
Entire Data	0.8219

Coefficients and mean R^2 values for CO_2 saturation

	b1	b2	b3	b4
Min	-1.0442	0.5578	-0.0082	-1.0453
Max	-0.9115	0.7255	0.0672	-0.7213
Mean	-0.9941	0.6030	0.0166	-0.9923
Std. Dev	0.0476	0.0416	0.0189	0.0654

	R^2
Test Data	0.9101
Train Data	0.9357
Entire Data	0.9315

With R^2 values > 0.9, Table S. 6 shows that MLR is better at predicting CO_2 saturation as compared to CO_2 capture efficiency. This suggests that the MLR model did not capture the complex, non-linear relationship to model system efficiency and motivated us to explore more complex machine learning algorithms.

Table S. 7: Mean R^2 values of the NN model over various train/test iterations.

Data Type	**CO_2 Capture Efficiency %**	**CO_2 Saturation %**
Test Data	0.955	0.990
Train Data	0.989	0.997
Entire Data	0.982	0.996

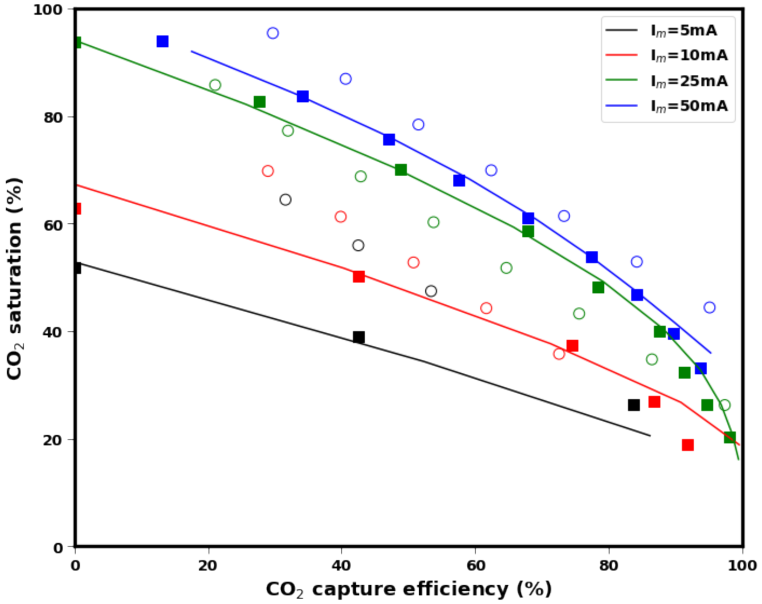

Figure S. 10: Comparison of prediction between COMSOL, MLR, and NN for CO_2saturation vs. CO_2 capture efficiency at a range of migration currents. Solid lines denote predictions using COMSOL, open circles represent MLR predictions, while solid squares indicate NN estimates.

Figure S. 10 shows the machine learning algorithms' prediction compared to the COMSOL data for CO_2saturation vs. CO_2 capture efficiency at various migration currents. Based on the figure, it can be inferred that the NN model closely resembles the COMSOL data while the MLR predictions deviate to a greater extent from the COMSOL data. At migration currents of 5 mA and 10 mA, the predictability of the MLR model is lower in comparison to that at the higher migration current, possibly due to the relatively few data points available at these conditions.Comparing the MLR results to NN, the NN model performs better in correlating the CO_2 capture efficiency and CO_2 saturation with R^2 reaching 0.95 and 0.99, respectively, as seen from Table S. 6, Table S. 7, Figure S. 11**,** and Figure S. 12**.**

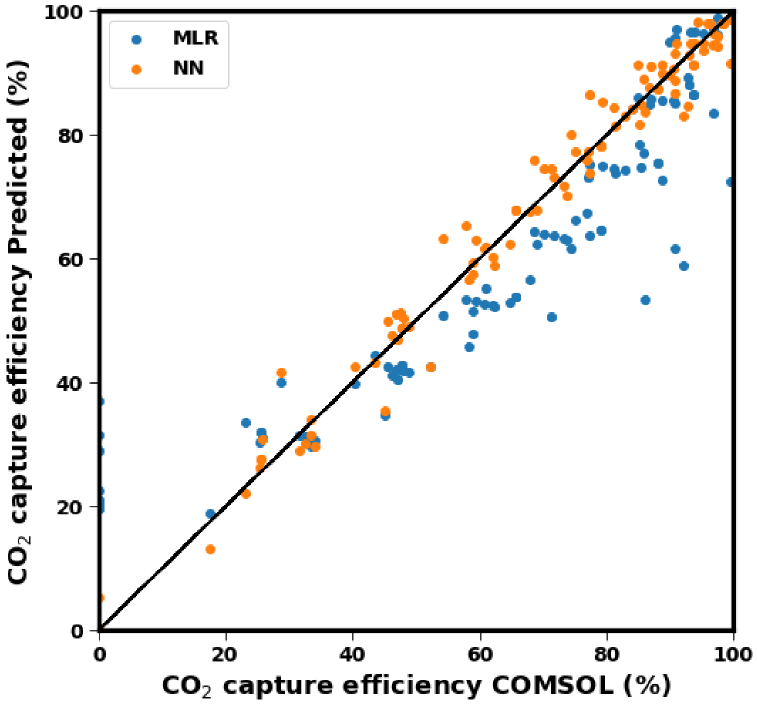

Figure S. 11: CO_2 capture efficiency % using MLR and NN in comparison with COMSOL data.

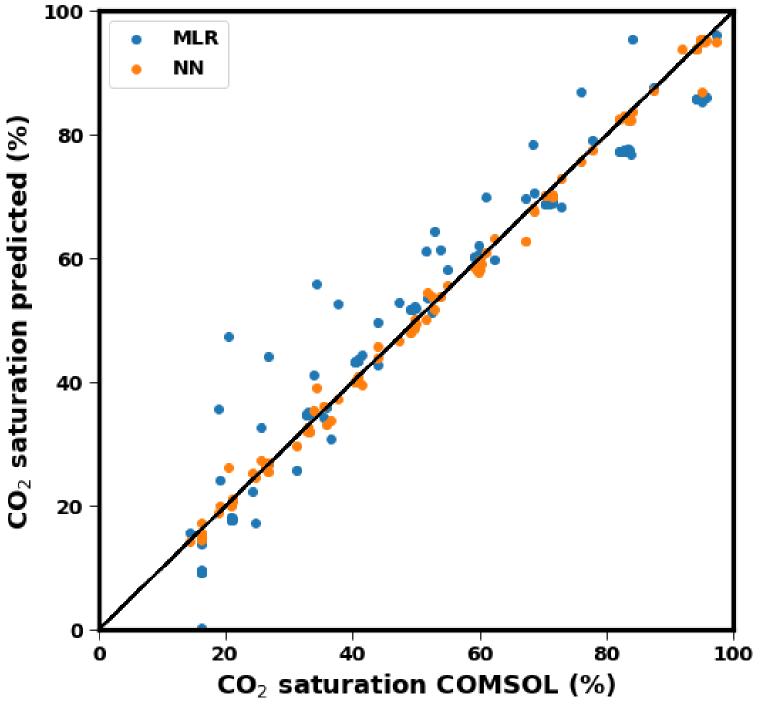

Figure S. 12: CO_2 saturation % using MLR and NN in comparison with COMSOL data.

This can be further seen in Figure S. 13 where the prediction is plotted for CO_2saturation % vs. CO_2 capture efficiency at various operating conditions. The NN predictions are very close to the COMSOL scatter points and, in some cases overlapping on top of each other, while the MLR predictions are scattered throughout the plot indicating that the operating condition and outputs exhibit complex non-linear behavior that is difficult to capture using MLR.

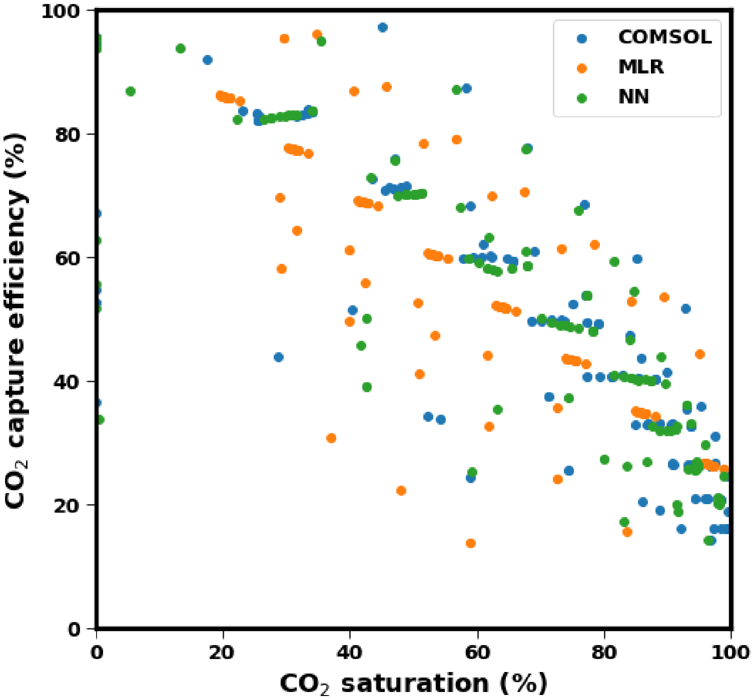

Figure S. 13: Comparison of prediction between COMSOL, MLR, and NN for CO_2 Saturation % vs. CO_2 capture efficiency %

Although the predictions from MLR models are not as accurate, the relative magnitude of feature coefficients of the linear regression model provides intuition about the relative contribution by each feature (Table S. 6). A positive coefficient indicates a direct correlation, whereas inverse correlation can be inferred from negative coefficients. Our study observed that CO_2 utilization current was the most significant feature in predicting CO_2 capture efficiency and CO_2 saturation, while membrane thickness was the least important feature. Further, based on the model coefficients, increased CO_2 utilization favored higher CO_2 capture efficiencies, thereby lowering CO_2 saturation.

References

1. Beck, Axel D. "Density-functional thermochemistry. III. The role of exact exchange." *J. Chem. Phys* 98.7 (1993): 5648-6.
2. Becke, Axel D. "A new mixing of Hartree–Fock and local density-functional theories.". *J. Chem. Phys* 98.2 (1993): 1372-1377.
3. Lee, Chengteh, Weitao Yang, and Robert G. Parr. "Development of the Colle-Salvetti correlation-energy formula into a functional of the electron density." *Physical review B* 37.2 (1988): 785.
4. Frisch, M. J. E. A., et al. "gaussian 09, Revision d. 01, Gaussian." *Inc., Wallingford CT* 201 (2009).
5. Tomasi, Jacopo, Benedetta Mennucci, and Roberto Cammi. "Quantum mechanical continuum solvation models." *Chemical reviews* 105.8 (2005): 2999-3094.
6. Jouyban, Abolghasem, and Shahla Soltanpour. "Prediction of dielectric constants of binary solvents at various temperatures." *Journal of Chemical & Engineering Data* 55.9 (2010): 2951-2963.
7. Flury, Markus, and Thomas F. Gimmi. "6.2 Solute Diffusion." *Methods of Soil Analysis: Part 4 Physical Methods* 5 (2002): 1323-1351.
8. Kiss, Andrew M., et al. "Carbonate and bicarbonate ion transport in alkaline anion exchange membranes." *Journal of The Electrochemical Society* 160.9 (2013): F994.
9. Huo, Sen, et al. "Water management in alkaline anion exchange membrane fuel cell anode." *International Journal of Hydrogen Energy* 37.23 (2012): 18389-18402.
10. Ternström, G., et al. "Mutual diffusion coefficients of water+ ethylene glycol and water+ glycerol mixtures." *Journal of Chemical & Engineering Data* 41.4 (1996): 876-879.
11. Hayduk, Walter, and Vinod K. Malik. "Density, viscosity, and carbon dioxide solubility and diffusivity in aqueous ethylene glycol solutions." *Journal of Chemical & Engineering Data* 16.2 (1971): 143-146.
12. Li, Y. S., T. S. Zhao, and W. W. Yang. "Measurements of water uptake and transport properties in anion-exchange membranes." *International Journal of Hydrogen Energy* 35.11 (2010): 5656-5665.
13. Weber, Adam Z., and John Newman. "Modeling transport in polymer-electrolyte fuel cells." *Chemical reviews* 104.10 (2004): 4679-4726.
14. Springer, Thomas E., T. A. Zawodzinski, and Shimshon Gottesfeld. "Polymer electrolyte fuel cell model." *Journal of The Electrochemical Society* 138.8 (1991): 2334.
15. Lin, Meng, et al. "An experimental-and simulation-based evaluation of the CO_2 utilization efficiency of aqueous-based electrochemical CO_2 reduction reactors with ion-selective membranes." *ACS Applied Energy Materials* 2.8 (2019): 5843-5850.
16. Sabatino, Francesco, et al. "Evaluation of a direct air capture process combining wet scrubbing and bipolar membrane electrodialysis." *Industrial & Engineering Chemistry Research* 59.15 (2020): 7007-7020.